Article Title: Enhanced Photoelectrochemical Detection of Alpha-Fetoprotein using Dipole Image Effect and Lock-In Amplification

Authors: Ting Yang[1 §], Douzhe Li[3 §], Aoqun Jian[1,2*], Huaping Jia[1,5], Dong Zhao[1], Yixia Zhang[4], Xuming Zhang[5*], and Shengbo Sang[1,2*]

Affiliation of authors:

1 Shanxi Key Laboratory of MicroNano Sensors & Artificial Intelligence Perception, College of Information and Computer, Taiyuan University of Technology, Taiyuan, 030024, China

2 Key Lab of Advanced Transducers and Intelligent Control System of the Ministry of Education, Taiyuan University of Technology, Taiyuan, 030024, China

3 Institute of Intelligent Perception and Internet of Things Technology, College of Information and Computer, Taiyuan University of Technology, Taiyuan, 030024, China

4 Department of Biomedical Engineering, Shanxi Key Laboratory of Material Strength & Structural Impact, College of Mechanics, Taiyuan University of Technology, Taiyuan 030024, China

5 Department of Applied Physics, The Hong Kong Polytechnic University, Hong Kong 999077, China

Running title: ACS Sensors

1st author: Ting Yang[1], Douzhe Li[2]

***Corresponding author:** Aoqun Jian[1*], Xuming Zhang[4*], and Shengbo Sang[1*]

Address: [1] Shanxi Key Laboratory of MicroNano Sensors & Artificial Intelligence Perception, College of Information and Computer, Taiyuan University of Technology, Taiyuan, 030024, China

Tel: +86-150-3440-5549;

E-mail: *jianaoqun@tyut.edu.cn*, *xuming.zhang@polyu.edu.hk*, *sangshengbo@tyut.edu.cn*

Enhanced Photoelectrochemical Detection of Alpha-Fetoprotein using Dipole Image Effect and Lock-In Amplification

Ting Yang[1 §], Douzhe Li[3 §], Aoqun Jian[1,2*], Huaping Jia[1,5], Dong Zhao[1], Yixia Zhang[4], Xuming Zhang[5*], and Shengbo Sang[1,2*]

1 Shanxi Key Laboratory of MicroNano Sensors & Artificial Intelligence Perception, College of Information and Computer, Taiyuan University of Technology, Taiyuan, 030024, China

2 Key Lab of Advanced Transducers and Intelligent Control System of the Ministry of Education, Taiyuan University of Technology, Taiyuan, 030024, China

3 Institute of Intelligent Perception and Internet of Things Technology, College of Information and Computer, Taiyuan University of Technology, Taiyuan, 030024, China

4 Department of Biomedical Engineering, Shanxi Key Laboratory of Material Strength & Structural Impact, College of Mechanics, Taiyuan University of Technology, Taiyuan 030024, China

5 Department of Applied Physics, The Hong Kong Polytechnic University, Hong Kong 999077, China

§ T.Y. and D.L contributed equally to this paper

KEYWORDS: photoelectrochemical, alpha-fetoprotein, dipole image effect, lock-in amplifier, AuNPs/TiO_2/Au sandwiched structure.

ABSTRACT: Alpha-fetoprotein (AFP) is a serum biomarker mainly for early-stage diagnosis and prognosis of primary liver cancer in clinical analysis. As a label-free analyte-specific biosensor with ultrahigh sensitivity and broad detection range, photoelectrochemical (PEC) sensor is promising for the AFP detection. A unique feature of the PEC sensor, the separation of its excitation source and the detection signal, offers a great opportunity in the spatial and temporal domain to enhance its performance. For the spatial domain, AuNPs/TiO_2/Au (in short, ATA) sandwiched structure was designed for magnetic resonance generation and light absorption enhancement. The strong light-matter interaction due to the dipole image effect has achieved a one-order-of-magnitude increase in the photocurrent response, the sensitivity and the signal-to-noise ratio (SNR) of the designed sensor. Instead of the typical method that manually switches the light source for photocurrent, an irradiation-modulated method (IMM) was proposed to modulate the light source in the temporal domain. Such modulated signal can be coherently amplified and extracted from a strong noise background, which improves the SNR of the photocurrent signal and leads to a larger measurement range. This designed AFP biosensor exhibited one-order-of-magnitude wider linear detection range from 10 pg mL^{-1} to 1 μg mL^{-1} with a detection limit of 4.5 pg mL^{-1}. Benefiting from simple preparation process, automated operation and markedly improved performance, this proposed PEC detection method can be promisingly used to enhance the performance of various PEC sensors for other proteins detections.

Hepatocellular carcinoma (HCC) is the most common and lethal form of liver cancer in adults with a poor early diagnosis and prognosis.[1-4] As a widely used tumor biomarker,[5-7] AFP has shown great promise in the early clinical diagnosis of HCC.[8] The average value of AFP concentration is 3.4 ng mL^{-1} in healthy adults' serum and is between 4.2 ng mL^{-1} and 520 ng mL^{-1} for HCC patients.[9-11] Therefore, the HCC early diagnosis and prognosis in clinical analysis requires the detection method of AFP concentration to have a high sensitivity and a wide linear range.

The photoelectrochemical (PEC) sensor is a rising method for various biological interactions.[12-14] It can probe photoelectron transfer processes at electrode-solution interfaces,[15] potentially achieving a higher sensitivity because its excitation source and the detection signal are separated.[16, 17] Furthermore, the low background noise and the fast, cost-effective detection process make it promising for the early clinical diagnosis.[18] AuNPs/TiO_2 is a promising photo-active composite material due to its high chemical stability and low toxicity.[13, 19-23] At present, a few PEC sensors based on AuNPs/TiO_2 have been successfully developed to specifically detect various analytes.[24-28] However, aiming at AFP concentration quantitative detection from various kinds of liquid biopsies (e.g., serum, saliva), the performance of the PEC sensor still needs further improvement.

Herein, according to the physical mechanism of the PEC sensor, its photocurrent (originated from incident irradiation) response, which is determined by the interaction between the chemical and biological analyte, can be enhanced in the spatial and temporal domains.

To enhance the light-matter interaction in the spatial domain, AuNPs/TiO_2/Au (in short, ATA) sandwiched nanocomposite film (see Figure 1(a)) was applied as an electrode for AFP analysis. The charge transfer of ATA-film is shown in Figure 1(b). Under the visible irradiation, the collectively oscillated electrons due to localized surface plasmon resonance (LSPR) generate hot electrons, which jump over the Schottky barrier formed at the metal-semiconductor interface to be injected into the nearby TiO_2 layer, and finally transfer to the Au layer and FTO substrate.[21, 24, 29, 30] Due to the dipole image effect generated by the proposed ATA electrode, magnetic resonance localized between AuNPs and Au film significantly enhances the light absorption and the photo-to-electric conversion efficiency. In the case of the temporal domain, the irradiation-modulated method (IMM) was proposed as a measurement strategy to

further boost the sensor performance. In IMM, the illumination of the light source was modulated by a reference signal in the temporal domain. And a lock-in amplifier was used to single out and amplify the component with the same frequency and phase as the reference signal. Thus, the signal-to-noise ratio (SNR) of the output signal can be significantly improved by differentiation and accumulation in the lock-in detection. The comparison of our sensor with other AFP sensors based on various sensing principles indicates that this sensing strategy is one of the best potential candidates for HCC early-stage diagnosis and prognosis in clinical analysis. Furthermore, with the merits of simple preparation process, automated operation and greatly enhanced performance, this proposed amplification strategy can be applied to various PEC sensors for other proteins.

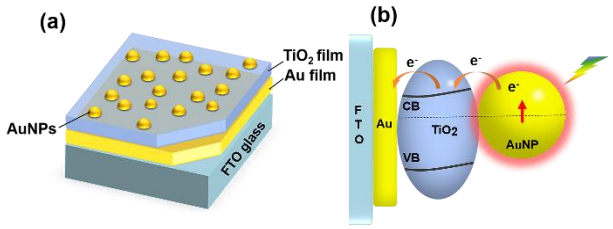

Figure 1. (a) ATA sandwiched structure. (b) Charge transfer mechanism of ATA-film.

Materials and Methods

Chemicals and materials

Antibody against alpha-fetoprotein (monoclonal) was purchased from Sangon Biotech (Shanghai) Co., Ltd Alpha-fetoprotein (AFP) was obtained from Shanghai Haling Biotechnology Co., Ltd. carcinoembryonic antigen (CEA) was obtained from Shanghai Linc-Bio Science Co. Ltd. (China). The FTO glass was purchased from NSG, Japan. 1-ethyl-3-(3-dimethylaminopropyl) carbodiimide hydrochloride (EDC), N-hydroxysulfosuccinimide (NHS), phosphate buffered saline (PBS, 0.01 M, pH = 7.4), and bovine serum albumin (BSA, 0.1%) were purchased from Sigma-Aldrich Corporation (Saint Louis, MO, USA). β-Mercaptoethylamine was purchased from Aladdin Reagents Ltd. All experiments used deionized water (18 mΩ resistivity).

Devices

The morphology and the element mapping of the samples were studied using a scanning electron microscope (SEM, JSM 5600) for energy dispersive spectroscopy (EDS). The optical absorption characteristics were studied by measuring the UV-visible absorption spectra using an ultraviolet-visible spectrophotometer (Shimadzu, UV-2600). The crystal structure of the sample was recorded by X-ray diffraction (XRD, Rigaku-D/max-2500). PEC measurements were carried on a CS2350H electrochemical workstation (Wuhan Corrtest Instruments Corp., Ltd) with a three-electrode system, the sample as the working electrode, a platinum wire as the counter-electrode, and a saturated Ag/AgCl electrode as the reference electrode. Finally, the experimental signals and the synchronization signal generated by the chopper (SR540，Stanford Research Systems) were collected by a lock-in amplifier (SR830, Stanford Research Systems) and were further recorded by a digital storage oscilloscope (DSO, GDS-2302A).

Preparation of ATA-film electrode

The ATA composite was fabricated according to the previous experimental method.[29] Firstly, the Au film was grown via magnetron sputtering on a glass substrate. Subsequently, TiO_2 sol-gel solution prepared according to the previous production method was deposited on the Au film surface by the spin coating of which speed was carefully adjusted to control the thickness of the TiO2 film.[31] To deposit AuNPs on the formed TiO_2 thin film, another Au film with 5 nm thickness was prepared by magnetron sputtering. After thermal annealing at 480℃ for 1 h,[32] AuNPs with uniform diameter were achieved.

Biochemical modification

The fabrication procedure of the sensor is shown in Figure 2. The sensor electrode washed by deionized water was immersed in β-Cysteamine solution (40 mM) and placed at room temperature in a dark environment for 12 h. After five rinses with deionized water, the unbound β -cysteamine was dried in a nitrogen stream. The antibody solution was mixed with PBS solution containing 4mg mL^{-1} EDC and 4mg mL^{-1} NHS in a 37°C shaker for 30min. The carboxyl group in the antibody was activated into NHS ester, which effectively combined with the amino group on the sensing electrode. Then the sensor was immersed in the activated antibody solution, placed under the incubator at 37°C for 1 h, and the antibody was uniformly fixed on the surface of the sensor electrode. To avoid electrostatic adsorption and steric hindrance between antibodies, the unbound and non-specific sites on the surface were sealed with 0.1% BSA for 30 min.

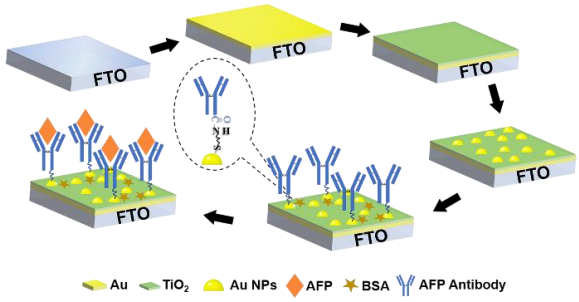

Figure 2. Fabrication procedures of ATA-film PEC sensor with AFP modification**.**

Photocurrent measurement based on IMM

The schematic graph of the IMM system is presented in Figure 3. Video of the IMM operations is provided in Supporting Information S1. In this method, the light source was modulated by an optical chopper. On one hand, the on/off of light source can generate a transistor-transistor logic (TLL) signal $V_{\mathrm{ls}}(t)$ which was sent into the lock-in amplifier then changed into a sinusoidal signal $V_{\mathrm{ref}}(t)$ for reference. On the other hand, as the irradiation was flashing at the electrode, a photocurrent signal $I_{in}(t)$ was generated and collected by the electrochemical workstation. $I_{in}(t)$ was also converted into a proportional voltage signal $V_{\mathrm{in}}(t)$ and can be obtained from the analog port of the electrochemical workstation.

Then, a phase-sensitive detection (PD) technique was used to detect and measure very small AC signals, i.e., $V_{in}(t)$, obscured by noise sources. The implementation of PD can be briefly described as the following three steps.

Firstly, $V_{\mathrm{in}}(t)$ and $V_{\mathrm{ref}}(t)$ are multiplied as

$$V_{\mathrm{psd}} = V_{\mathrm{in}}(t)V_{\mathrm{ref}}(t) \quad (1)$$

As any signal can be decomposed into several sinusoidal components according to the Fourier theory, $V_{\text{in}}(t)$ is represented by only one of these sinusoidal components, i.e., $V_{\text{in}}(t) = A_{\text{in}}sin(\omega_{\text{in}}t + \theta_{\text{sig}})$. Besides, assume the reference $V_{\text{ref}}(t)$ can be represented as $V_{\text{ref}}(t) = A_{\text{ref}}sin(\omega_{\text{ref}}t + \theta_{\text{ref}})$. For both $V_{\text{in}}(t)$ and $V_{\text{ref}}(t)$, A ω,θ are amplitude, frequency and phase of a sinusoidal signal, respectively. Then, Eq. (1) is transformed to Eq. (2)

$$V_{\text{PD}} = \frac{1}{2}A_{\text{in}}A_{\text{ref}}cos[(\omega_{\text{in}} - \omega_{\text{ref}})t + (\theta_{\text{in}} - \theta_{\text{ref}})]- \frac{1}{2}A_{\text{in}}A_{\text{ref}}cos[(\omega_{\text{in}} + \omega_{\text{ref}})t + (\theta_{\text{in}} + \theta_{\text{ref}})] \quad (2)$$

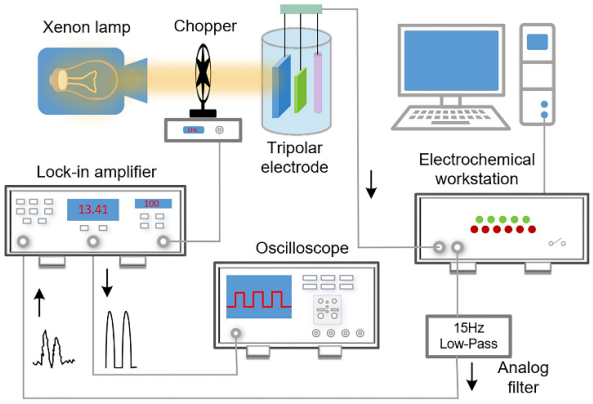

Figure 3. Schematic diagram of the IMM.

Obviously V_{PD} has two AC signal components, one at difference frequency $\omega_{\text{in}} - \omega_{\text{ref}}$ and the other at sum frequency $\omega_{\text{in}} + \omega_{\text{ref}}$. Since the on/off time of chopper is in the order of seconds and the response time of electrode is in the order of picoseconds, the difference between these two time scales is about 12 orders of magnitude, so the response speed of the electrode is fast enough and ω_{in} is considered to be identical to ω_{ref}.

Secondly, by passing a low-pass filter to remove the sum frequency component, also taking into account that $\omega_{\text{in}} = \omega_{\text{ref}}$, V_{PD} is transformed to V'_{PD} and can be expressed as

$$V'_{\text{PD}} = \frac{1}{2}A_{\text{in}}A_{\text{ref}}cos(\theta_{\text{in}} - \theta_{\text{ref}}) \quad (3)$$

Thirdly, to eliminate $\theta_{\text{in}} - \theta_{\text{ref}}$, another PD signal $V''_{\text{PD}} = 1/2A_{\text{in}}A_{\text{ref}}sin(\theta_{\text{in}} - \theta_{\text{ref}})$ can be obtained according to the internal algorithm of the lock-in amplifier following the similar procedure of Eq. (1), but with an additional 90° phase shift of $V_{\text{ref}}(t)$. The overall output of lock-in amplifier R is

$$R = \sqrt{{V'_{PD}}^2 + {V''_{PD}}^2} = \frac{1}{2}A_{\text{in}}A_{\text{ref}} \quad (4)$$

In the ideal case, R only contains the DC component. However, as limited by accuracy of the cut-off frequency of lock-in amplifier's internal filter, the AC component cannot be completely removed, thus R is still a time variant signal and should be further processed by an external digital low-pass filter $F(n)$. The output of filter $F(n)$ is denoted by $y(n)$. Since the modulation frequency (i.e., f_{ref}) was set at 1.8 Hz to avoid insufficient current response, the cut-off frequency of $F(n)$ was set as 3 Hz to effectively suppress the 2nd and higher order harmonics of 1.8 Hz. For details of parameter settings, see Supporting Information S3.

In Figure 4, $y(n)$ was repeatedly measured by peak-to-peak values in several consecutive time spans that each contains at least two periods (when $f_{\text{ref}} = 1.8$ Hz, two periods of $y(n)$ equals 1.1 s). Although more repeated measurements and the average operation would give more accurate results, in our experiments, relatively stable results can be obtained after 2 - 3 periods. Furthermore, a more exciting discovery is that the current spike during the light source on/off switching due to the charge recombination can be easily removed. In addition, the automatic operation of the proposed IMM method paves the road to more stable and accurate results.

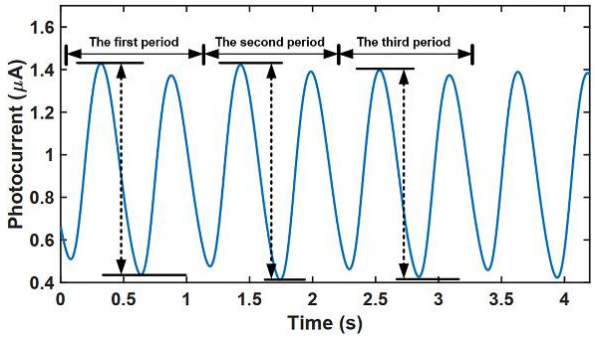

Figure 4. Overall output of the lock-in amplifier in temporal domain. The signal is highly periodic.

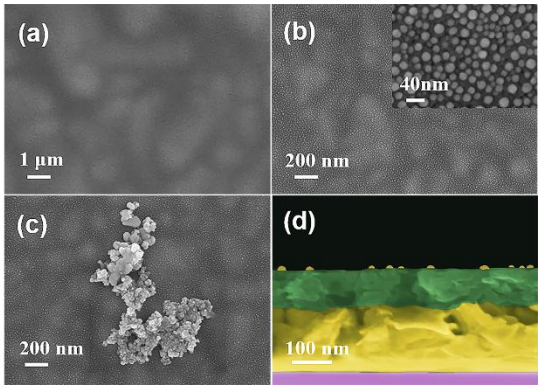

Figure 5. SEM images of TiO_2/Au-film/FTO (a), ATA/FTO (b), anti-AFP/ATA-film /FTO (c), and cross-section of the prepared ATA-film/FTO (d). The inset of (b) shows the enlarged view of AuNPs.

Results and Discussion

Characterization of the modified electrode

The surface and lateral morphologies of the PEC sensor electrode were characterized by SEM. It can be found that the surface of the fabricated TiO_2/FTO electrode (Figure 5(a)) is uniform and relatively smooth. After the deposition of AuNPs, the nearly-spherical AuNPs are uniformly distributed on the surface of TiO_2 film (Figure 5(b)). After the surface modification of AFP antibodies, biological macromolecules appear on the electrode (Figure 5(c)). The cross-section of the fabricated ATA structure presents a multilayer structure on the FTO substrate (Figure 5(d)). Additionally, the EDS data in Figure 6 shows that Ti, O, and Au signals were detected from the ATA, indicating that the composite consists of TiO_2 and Au.

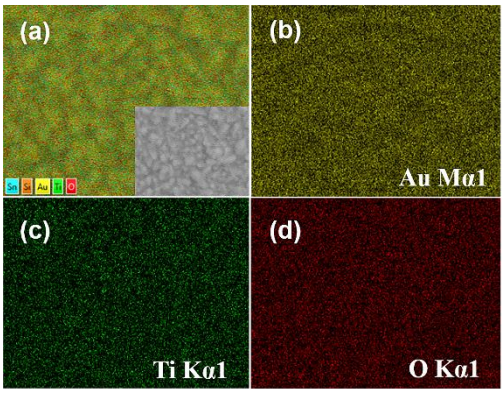

Figure 6. EDS mapping images of ATA-film/FTO for Au (a), Au (b), Ti (c), and O (d).

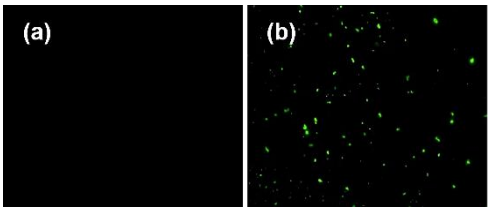

Figure 7. Fluorescence images of the control experiment (a) and the anti-AFP-FITC modified on the biosensor surface (b).

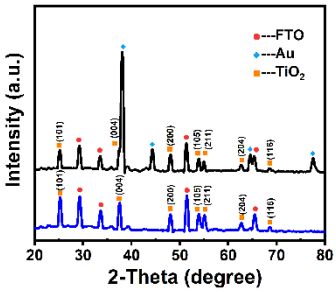

Figure 8. X-ray diffraction patterns of TiO_2/FTO (blue line), and ATA-film/FTO (black line).

Fluorescein isothiocyanate (FITC) can react with the amino group of the protein to label the fluorescein AFP antibody. As shown in Figure 7(b), green fluorescence spots uniformly cover the whole area. As the control, the electrode without fixed antibody presents no green fluorescence points under the same conditions as shown in Figure 7(a). The results indicate that the AFP antibodies had been successfully incubated on the electrode surface. After the optimization of the incubation time and the electrolyte pH, a high-performance electrode for the PEC sensor was prepared (see Figures S1 and more details in the Supporting Information S2).

Figure 8 shows the crystal structure of the ATA composite film by XRD. The red diffraction peak represents the FTO substrate, all the diffraction peaks at angles 25.35°, 37.78°, 48.07°, 53.92°, 55.11°, 62.72°, and 68.594° (marked by orange dots) for the TiO_2 can be perfectly indexed as the anatase TiO_2, respectively (JCPDS no. 04-0477).[33]The peaks (marked by blue dots) at 2θ = 38.05°, 44.39°, 64.58°, and 77.56° are the crystal planes of Au (JCPDS no. 02-1095).[34]

Realization of dipole mirror effect

To understand the mechanism of broadband optical absorption of ATA sandwiched structure, the electric and magnetic field distributions were simulated by the three-dimensional finite-difference time-domain (FDTD) method. In this work, two types of models: AuNPs/TiO_2 and ATA structure were investigated when the TiO_2 film between the Au film and AuNPs has different thickness (thickness = 20 – 100 nm, marked as T20 – T100). As shown in Figure 9, with the increase of TiO_2 thickness, strong magnetic field gradually appeared in the TiO_2 layer and gold film due to magnetic resonance.[35-37] The ATA-film (T70) has the strongest magnetic resonance, which indicates an extremely strong irradiation absorption due to the image dipole effect.[38] When the thickness of the TiO_2 interlayer continued to rise (100 nm), the area and intensity of the magnetic field dropped significantly, suggesting a decrease in energy absorption. Moreover, a local enhanced electric field can be observed in the bottom tips of AuNPs, of which intensity shares the same trend with that of the magnetic field. The strong electric and magnetic field of the ATA sandwiched structure greatly enhance the absorption of light, further contributes to the improvement of the photocurrent.[39] Such phenomenon is consistent well with some previous studies.[38, 40] According to the simulation analysis above, the thickness of TiO_2 film was chosen as 70 nm in the ATA sandwiched structure in the following experiments.

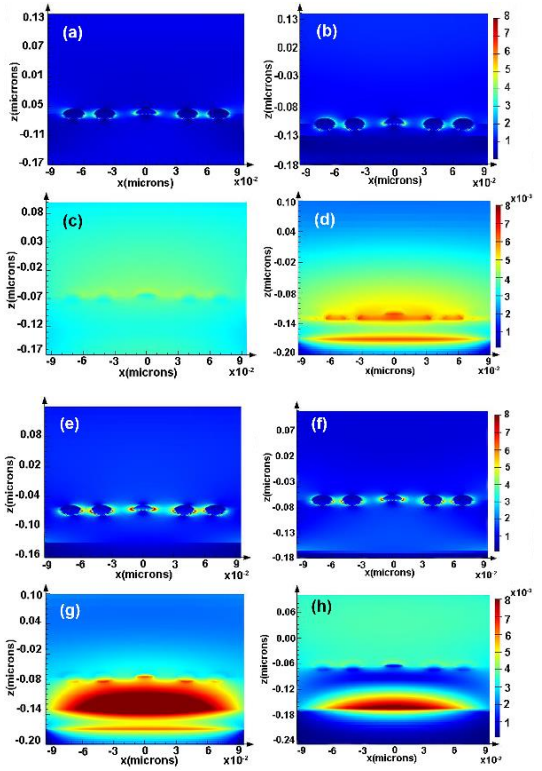

Figure 9. FDTD simulated results. The electric field distributions of AuNPs/TiO_2 (a), and ATA-film with different TiO_2 thicknesses (T20 (b), T70 (e), T100 (f)), and the magnetic field distributions of AuNPs/TiO_2 (c), ATA-film with different TiO_2 thicknesses (T20 (d), T70 (g), T100 (h)).

The enhancement of light absorption was further demonstrated by UV-vis absorption spectroscopy (see Figure 10). It can be seen that the pure TiO_2 layer little absorption of visible light, and AuNPs/TiO_2 composite exhibits an absorbance peak at approximately 540 nm, which is attributed to the LSPR of the AuNPs. The purple line is for the ATA sandwiched nanocomposite film (T20), and is significantly enhanced compared with that of AuNPs/TiO_2. Furthermore, when the thickness of the

TiO_2 layer is increased to 70 nm (T70, blue line), the absorption is further enhanced. The enhanced light absorption paves the way to the improvement of photoelectric response and the optimization of SNR.

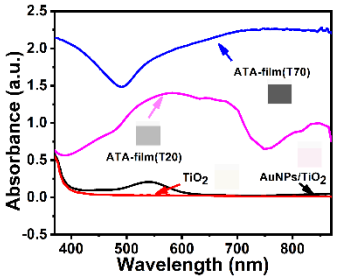

Figure 10. UV-vis absorption spectra of TiO_2, AuNPs/TiO_2, ATA films with different TiO_2 thicknesses (T20, T70).

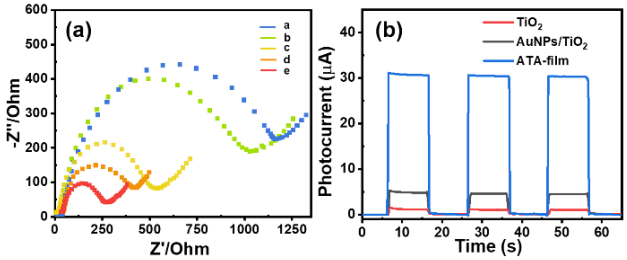

Figure 11. (a) EIS spectra of a series of photoelectrodes (AFP/anti-AFP/ATA-film(a), anti-AFP/ATA-film(b), TiO_2(c), AuNPs/TiO_2(d), ATA-film(e)). (b) Photocurrent responses of TiO_2 film, AuNPs/TiO_2 film and ATA-film.

Photoelectrochemical and EIS performance

Figure 11(a) shows the EIS spectra of the PEC electrodes on different stages of the assembly process, and reveals the electron transport on the electrode surface. It can be found that the TiO_2/FTO electrode (yellow line) shows a relatively small resistance. After AuNPs were deposited on the TiO_2 film surface, the diameter decreases (orange line), which indicates that AuNPs can promote charge transport. The observed diameter of ATA-film (red line) in the EIS spectrum is the smallest, suggesting higher conductivity and larger charge transfer efficiency compared with other electrodes. After the incubation of the AFP antibody on the electrode (green line), the diameter of the semicircular curve is increased, which is due to the non-conductive effect of the AFP antibody. As the photoelectric chemical sensing electrode was incubated with the target antigen (blue line), it resulted in a further increase of the diameter, showing the successful binding between the AFP antigen and the antibody.

Photoelectric response enhancement of ATA-film was further demonstrated in the photocurrent investigation. Figure 11(b) shows that no significant photocurrent changes are observed during the on-off cycles of the TiO_2/FTO electrode. After the deposition of AuNPs, the photocurrent signal response is 5-fold that of the original TiO_2 film due to the injection of hot electrons from the LSPR-excited AuNPs to TiO_2. When the Au film was added between the TiO_2 thin film and the FTO glass, because of the dipole image effect as shown in the FDTD study, the photocurrent density is significantly increased to 30 μA, more than 6-times that of the AuNPs/TiO_2 electrode. Such an enormous growth of photocurrent paves a way to improving the performance of the ATA sensor (see detailed analyses below).

Power spectral density analysis and SNR calculation

The raw signal $V_{\text{in}}(t)$ in Figure 12(a) was obtained from the analog port of electrochemical-workstation, processed by a lock-in amplifier (Figure 12(b)), and then filtered by a 3-Hz low-pass digital filter for harmonics suppression (Figure 12(c)). Intuitively, the noise is mitigated and the signal is gradually smoothed by our proposed method.

The corresponding power spectral density (PSD) of the signals in Figure 12 (a)-(c) are given in Figure 12 (d)-(f). In Figure 12(d), the 1.8-Hz fundamental frequency and its 2nd harmonic have almost the same power level, and the 3rd-5th harmonics and the 50-Hz noise are presented as well. After using our proposed IMM method, all orders of harmonics and the 50-Hz noise are significantly suppressed (Figure 12(f)). For quantitative analysis, according to the theory of PSD, the detailed SNR was calculated by Eq. (4) and listed in Table 1.

$$SNR = 10\log_{10}\frac{\sum_{f=1.8} PSD}{\sum_{f\neq 1.8, f\neq 0} PSD} \quad (4)$$

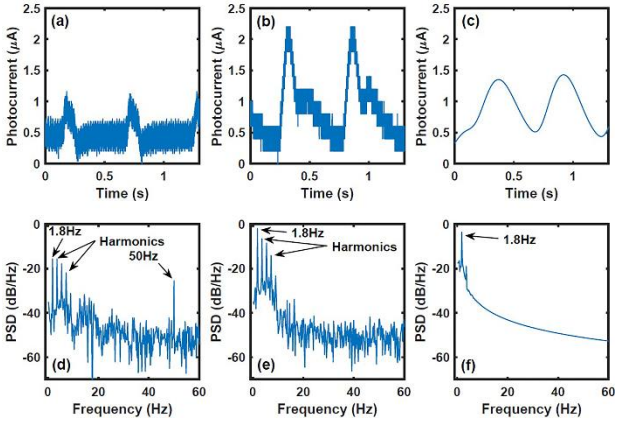

Figure 12. Signal processing stages of (a) raw signal, (b) lock-in amplifier, (c) digital filter, and the corresponding power spectral densities of raw signal (d), lock-in amplifier (e), digital filter (f).

Table 1. SNR analysis of different signal processing stages

Stages	Signal (dB)	Harmonics (dB)	50-Hz Noise (dB)	SNR (dB)
$V_{\text{in}}(t)$	-15.69	2nd order -15.74 3rd order -17.88 4th order -21.98	-25.57	-3.15
Lock-in amplifier & 50-Hz mitigation	-2.04	2nd order -6.60 3rd order -8.56 4th order -14.16	-43.24	1.97
Smoothed	-3.63	2nd order -19.03 3rd order -32.01 4th order -34.36	-53.18	14.54

It can be seen from Table 1 that the IMM improves the SNR by about 17.7 dB (from -3.15 dB to 14.54 dB, about 59 times). The signal power is boosted by 13 dB (from -15.69 dB to -2.04 dB, about 20 times) after passing through the lock-in amplifier since the magnitude of a specific frequency is amplified by a factor of $1/2\ A_{\text{ref}}$ (see Eq. (4)). Moreover, the signal power is lowered a bit after passing through the digital low-pass filter as caused by the passband gain of digital filter. Actually, in each

experiment, the overall amplification factor was calibrated before the data recording to get the accurate result.

In the typical PEC sensors, before recording and processing data by the build-in software of electrochemical workstation, the on/off of light source was often manually controlled with the typical period of 20 s for signal stabilization. A sample signal and its corresponding PSD are shown in Figure 13.

Since a quasi-square signal contains rich harmonic components, the 2^{nd}-8^{th} harmonics of 0.05 Hz existed inherently. Using the same calculation equation in Eq. (4), the SNR is 7.37 dB, about 7 dB (5 times) worse than our proposed method. Moreover, since the 0.05-Hz fundamental frequency and its harmonics are too close to separate by a low-pass filter, the harmonics (< 0.1 Hz) are more difficult to suppress in this case. In addition, the on/off time of light source and the stability of photocurrent response depend on subjective judgment and is prone to error.

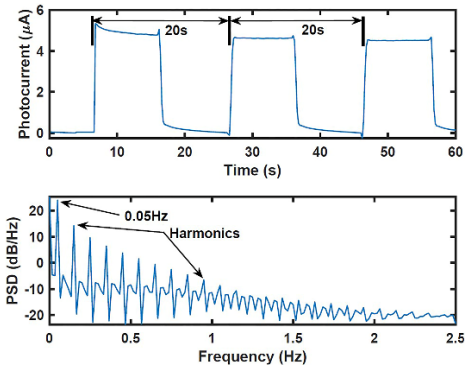

Figure 13. A sample signal recorded by typical method and its corresponding PSD.

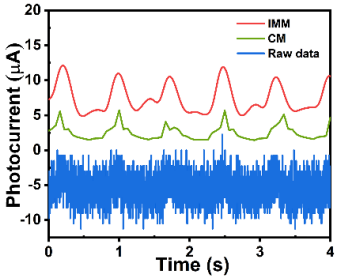

Figure 14. A comparison of signal responses among our proposed irradiation-modulated method (IMM), the conventional method (CM) and the original data (raw data).

The comparison of signal quality between the proposed IMM method and the typical method are presented in Figure 14. When the concentration of the analyte is increased, due to the continuously increase in the resistance of the electrode, the raw photocurrent signal collected from the analog port of the electrochemical workstation is overwhelmed by the strong noise (blue line). It is difficult to identify the desired signal $V_{\text{in}}(t)$. By the signal amplification and processing method built in the lock-in amplifier, most of the noise is removed (green line), but the shoulder parts of the quasi-square signal are severely blurred, making it almost undiscernible. To make it worse, the signal was interfered by the strong spikes. The photocurrent signal processed by our proposed IMM is clearly presented and spike-free (red line), and the quasi-sine current response can be easily measured by the peak-to-peak detection method (see Figure 4).

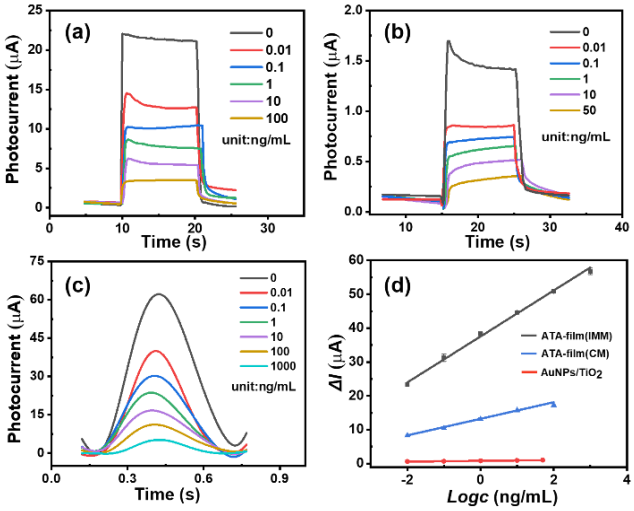

Figure 15. Photocurrent responses of the sensors based on the ATA sandwiched structure (a), the AuNPs/TiO_2 structure (b), and the ATA sandwiched structure using the IMM method for the detection of different concentrations of AFP (c). Linear fits of the logarithm of the AFP concentration C and the photocurrent ΔI (d). Error bars show the standard deviation of five repeated measurements.

Table 2. Comparison of the performances of the PEC sensors with different electrodes

Electrodes	Linear range (ng/mL)	Detection limit (pg/mL)	Linear equation	R^2
AuNPs/TiO_2	10^{-2}-50	59.45	I = 0.81 + 0.11 log$C$	0.991
ATA-film (CM)	10^{-2}-10^{2}	20.06	I = 13.23 + 2.45 log$C$	0.992
ATA-film (IMM)	10^{-2}-10^{3}	4.5	I = 44.32 + 6.79 log$C$	0.997

Table 3. Comparison of various methods for AFP detection

Analytical techniques	Linear range (ng/mL)	Detection limit (pg/mL)	Ref.
Fluorescence aptasensor	0.5-60	160	[41]
Resonance light scattering sensor	5.0-100	940	[42]
Photoelectrochemical immunosensor	0.05-20	14.7	[43]
Photoelectrochemical sensor	0.01-1000	4.5	this work

Photoelectrochemical detection of AFP antigen

Figure 15(a) presents the photocurrent responses of the designed ATA-film electrode after being incubated with different concentrations of the target protein. The photocurrent gradually decreases with the increase of AFP concentration. AuNPs/TiO_2 electrodes were also measured under the same experimental condition for comparison (Figure 15(b)). It can be found that the dipole image effect resulted in a 14-fold increase in photocurrent at the ATA sensor compared with Au/TiO_2 (22 μA vs 1.5 μA). And the enhancement of photocurrent tremendously

improved the sensitivity of the ATA-film sensor by over 20 times (see Table 3).

Furthermore, the ATA sandwiched sample was sequentially tested in this section with the IMM. Here, the voltage signal outputted from the lock-in amplifier was converted into the current value for comparison. The peak-to-peak value of sinusoidal signals also gradually decreased as the AFP concentration increased. As the SNR of the photocurrent signal is remarkably enhanced by the ATA-film (T70) combined with the IMM, the sensitivity rises by over 2 times with a detection limit of 4.5 pg mL^{-1}, and the detection range is increased by one order of magnitude. As shown in Figure 15(d), there is an excellent linear relationship between the photocurrent and the logarithm of AFP concentration. The detailed parameters are listed in See Table 2. Compared with the other AFP detection methods, this designed PEC sensor exhibits a wider detection range and a lower detection as can be seen from Table 3.

3.5. Specificity, reproducibility and stability of the sensor

The specificity of the designed AFP sensor was investigated by exposure of the anti-AFP/ATA-film/FTO electrode to different types of proteins, including the target protein AFP, the carcinoembryonic antigen (CEA), the human chorionic gonadotropin (HCG) and the bovine serum albumin (BSA), all have the same concentration 10 ng mL^{-1}. As shown in Figure 16(a), no distinct changes in photocurrent response are observed by exposing the sensor to CEA, HCG, and BSA antigen. However, a significant photocurrent is obtained under the same experimental conditions when the antibody and AFP antigen are incubated. At the same time, there are noteworthy differences between the AFP antigen and the other antigen groups ($P < 0.001$). The results verify that the proposed PEC sensor has excellent selectivity for AFP antigen.

The reproducibility of the designed sensor was investigated by comparing the 0.01 ng mL^{-1} AFP antigen detection results of five new modified electrodes (Figure 16(b)). The relative standard deviation is 1.79%, suggesting an acceptable reproducibility for AFP antigen detection. The stability of the AFP sensor was also examined. After being stored at 4°C for two weeks, only a slight drop of photocurrent response is observed, indicating an excellent stability of the designed sensor.

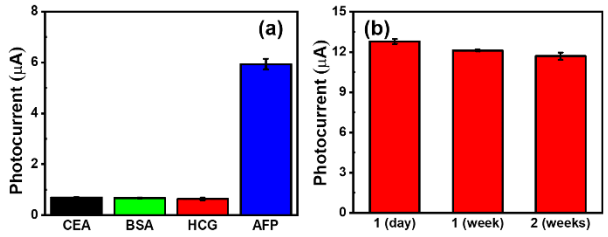

Figure 16. Measured specificity and stability of the PEC sensor for AFP detection. (a) Photocurrent responses of the ATA structure sensor to AFP and other proteins ($P < 0.001$). (b) Stability evaluation of the ATA structure sensor for detecting 0.01 ng mL^{-1}. Error bars show the standard deviation of 5 repeated tests.

CONCLUSION

In this paper, the performance enhancement of a PEC sensor for label-free AFP detection has been realized in spatial and temporal domains. An ATA electrode uses the sandwiched structure of AuNPs, TiO_2 and Au film to enhance the light-matter interaction in the spatial domain, and thus results in significant enhancement of light absorption due to the dipole image effect. Regarding the temporal domain, the IMM method is employed to improve the SNR of the photocurrent. Compared with the typical PEC sensors using the classical Au/TiO_2 electrode and the manual operation, the sensitivity and the measurement range of the designed sensor are increased by over 60 and 20 times, respectively. And its detection limit can reach as low as 4.5 pg mL^{-1}. The superior performance of our sensor as compared to other reported AFP sensors using various sensing principles suggests a bright prospect for its applications in photoelectrochemical biosensors.

ASSOCIATED CONTENT

Supporting Information

A video of operation process of the IMM; incubation condition optimization with pH and incubation time; Detailed parameters of lock-in amplifier.

AUTHOR INFORMATION

Corresponding Author

Aoqun Jian - https://orcid.org/0000-0002-6532-7595; Email: jianaoqun@tyut.edu.cn

Xuming Zhang - https://orcid.org/0000-0002-9326-5547; Email: xuming.zhang@polyu.edu.hk

Shengbo Sang - https://orcid.org/0000-0003-4974-9306; Email: sangshengbo@tyut.edu.cn

ACKNOWLEDGMENT

The research was partially supported by the National Natural Science Foundation of China (No.61501316, 51505324, 62031022), Excellent Talents Technology Innovation Program of Shanxi Province of China (201805D211020), the Natural Science Foundation for Young Scientists of Shanxi Province, China (201801D221184), and the Research Grants Council (RGC) of Hong Kong (15218415, 15212717, 15212618, 15221919E, 15215620E, N_PolyU511/20).

REFERENCES

(1) Yang, J. D.; Roberts, L. R., Hepatocellular carcinoma: a global view. *Nat. Rev. Gastroenterol. Hepatol.* **2010,** *7* (8), 448-458.

(2) Marrero, J. A., Hepatocellular carcinoma. *Curr. Opin. Gastroenterol.* **2006,** *22* (3), 248-253.

(3) Song, S.; Yang, Y. X.; Liu, M. H.; Liu, B. Y.; Yang, X.; Yu, M.; Qi, H.; Ren, M. M.; Wang, Z.; Zou, J. H.; Li, F.; Due, X. J.; Zhang, H. Q.; Luo, J. Y., MiR-125b attenuates human hepatocellular carcinoma malignancy through targeting SIRT6. *Am. J. Cancer Res.* **2018,** *8* (6), 993-1007.

(4) Lim, T. S.; Kim, D. Y.; Han, K.-H.; Kim, H.-S.; Shin, S. H.; Jung, K. S.; Kim, B. K.; Kim, S. U.; Park, J. Y.; Ahn, S. H., Combined use of AFP, PIVKA-II, and AFP-L3 as tumor markers enhances diagnostic accuracy for hepatocellular carcinoma in cirrhotic patients. *Scand. J. Gastroenterol.* **2016,** *51* (3), 344-353.

(5) Zhang, G.; Ha, S.-A.; Kim, H. K.; Yoo, J.; Kim, S.; Lee, Y. S.; Hur, S. Y.; Kim, Y. W.; Kim, T. E.; Park, Y. G.; Wang, J.; Yang, Y.; Xu, Z.; Song, E. Y.; Huang, Z.; Peng, J.; Jin, Z.; Qiao, S.; Cui, Z.; Lei, G.; Kim, J. W., Combined analysis of AFP and HCCR-1 as an useful serological marker for small hepatocellular carcinoma: A prospective cohort study. *Dis. Markers* **2012,** *32* (4), 265-271.

(6) Ge, T.; Shen, Q.; Wang, N.; Zhang, Y.; Ge, Z.; Chu, W.; Lv, X.; Zhao, F.; Zhao, W.; Fan, J.; Qin, W., Diagnostic values of alpha-fetoprotein, dickkopf-1, and osteopontin for hepatocellular carcinoma. *Med. Oncol.* **2015,** *32* (3).

(7) Lou, J.; Zhang, L.; Lv, S.; Zhang, C.; Jiang, S., Biomarkers for Hepatocellular Carcinoma. *Biomarkers Cancer* **2017,** *9*, 1-9.

(8) Chao, Z.; Zhang, J.; Wang, J.; Yan, Y.; Zhang, C., Alpha-fetoprotein accelerates the progression of hepatocellular carcinoma by promoting Bcl-2 gene expression through an RA-RAR signalling pathway. *J. Cell. Mol. Med.* **2020,** *24* (23), 13804-13812.

(9) Yang, Z.; Fu, Z.; Yan, F.; Liu, H.; Ju, H., A chemiluminescent immunosensor based on antibody immobilized carboxylic resin beads coupled with micro-bubble accelerated immunoreaction for fast flow-injection immunoassay. *Biosens. Bioelectron.* **2008,** *24* (1), 35-40.

(10) Cao, Y.; Yuan, R.; Chai, Y.; Mao, L.; Niu, H.; Liu, H.; Zhuo, Y., Ultrasensitive luminol electrochemiluminescence for protein detection based on in situ generated hydrogen peroxide as coreactant with glucose oxidase anchored AuNPs@MWCNTs labeling. *Biosens. Bioelectron.* **2012,** *31* (1), 305-309.

(11) Niu, H.; Yuan, R.; Chai, Y.; Mao, L.; Yuan, Y.; Zhuo, Y.; Yuan, S.; Yang, X., Electrochemiluminescence of peroxydisulfate enhanced by L-cysteine film for sensitive immunoassay. *Biosens. Bioelectron.* **2011,** *26* (7), 3175-3180.

(12) Zhao, W.-W.; Xu, J.-J.; Chen, H.-Y., Photoelectrochemical bioanalysis: the state of the art. *Chem. Soc. Rev.* **2015,** *44* (3), 729-741.

(13) Zhao, W.-W.; Xu, J.-J.; Chen, H.-Y., Photoelectrochemical DNA Biosensors. *Chem. Rev.* **2014,** *114* (15), 7421-7441.

(14) Qiu, Z.; Tang, D., Nanostructure-based photoelectrochemical sensing platforms for biomedical applications. *J. Mater. Chem. B* **2020,** *8* (13), 2541-2561.

(15) Zhang, X.; Guo, Y.; Liu, M.; Zhang, S., Photoelectrochemically active species and photoelectrochemical biosensors. *RSC Adv.* **2013,** *3* (9), 2846-2857.

(16) Li, X.; Wang, X.; Zhang, L.; Gong, J., High-Throughput Signal-On Photoelectrochemical Immunoassay of Lysozyme Based on Hole-Trapping Triggered by Disintegrating Bioconjugates of Dopamine-Grafted Silica Nanospheres. *ACS Sens.* **2018,** *3* (8), 1480-1488.

(17) Guo, L.; Yin, H.; Xu, M.; Zheng, Z.; Fang, X.; Chong, R.; Zhou, Y.; Xu, L.; Xu, Q.; Li, J.; Li, H., In Situ Generated Plasmonic Silver Nanoparticle-Sensitized Amorphous Titanium Dioxide for Ultrasensitive Photoelectrochemical Sensing of Formaldehyde. *ACS Sens.* **2019,** *4* (10), 2724-2729.

(18) Zhuang, J.; Tang, D.; Lai, W.; Xu, M.; Tang, D., Target-Induced Nano-Enzyme Reactor Mediated Hole-Trapping for High-Throughput Immunoassay Based on a Split-Type Photoelectrochemical Detection Strategy. *Anal. Chem.* **2015,** *87* (18), 9473-9480.

(19) Liu, X.-P.; Chen, J.-S.; Mao, C.-j.; Niu, H.-L.; Song, J.-M.; Jin, B.-K., Enhanced photoelectrochemical DNA sensor based on TiO2/Au hybrid structure. *Biosens. Bioelectron.* **2018,** *116*, 23-29.

(20) Bora, T.; Zoepfl, D.; Dutta, J., Importance of Plasmonic Heating on Visible Light Driven Photocatalysis of Gold Nanoparticle Decorated Zinc Oxide Nanorods. *Sci. Rep.* **2016,** *6*.

(21) Cho, S.; Yim, G.; Park, J. T.; Jang, H., Surfactant-free one-pot synthesis of Au-TiO2 core-shell nanostars by inter-cation redox reaction for photoelectrochemical water splitting. *Energy Convers. Manage.***2021**.

(22) Yan, X. X.; Li, J. J.; Yang, R. Y.; Li, Y. M.; Zhang, X. H.; Chen, J. H., A new photoelectrochemical aptasensor for prion assay based on cyclodextrin and Rhodamine B. *Sens. Actuators, B* **2018,** *255*, 2187-2193.

(23) Zhang, Z.; Zhang, L.; Hedhili, M. N.; Zhang, H.; Wang, P., Plasmonic Gold Nanocrystals Coupled with Photonic Crystal Seamlessly on TiO2 Nanotube Photoelectrodes for Efficient Visible Light Photoelectrochemical Water Splitting. *Nano Lett.* **2013,** *13* (1), 14-20.

(24) Ko, W. Y.; Tien, T. J.; Hsu, C. Y.; Lin, K. J., Ultrasensitive label- and amplification-free photoelectric protocols based on sandwiched layer-by-layer plasmonic nanocomposite films for the detection of alpha-fetoprotein. *Biosens. Bioelectron.* **2019,** *126*, 455-462.

(25) Guo, L.; Li, Z.; Marcus, K.; Navarro, S.; Liang, K.; Zhou, L.; Mani, P. D.; Florczyk, S. J.; Coffey, K. R.; Orlovskaya, N.; Sohn, Y.-H.; Yang, Y., Periodically Patterned Au-TiO2 Heterostructures for Photoelectrochemical Sensor. *ACS Sens.* **2017,** *2* (5), 621-625.

(26) Zhang, X. D.; Yue, D.; Zhang, L.; Lin, S. W., Three-dimensional flexible Au nanoparticles-decorated TiO2 nanotube arrays for photoelectrochemical biosensing. *J. Mater. Sci. Technol.* **2020,** *56*, 162-169.

(27) Chen, Y.; Li, Y.; Deng, D.; He, H.; Yan, X.; Wang, Z.; Fan, C.; Luo, L., Effective immobilization of Au nanoparticles on TiO2 loaded graphene for a novel sandwich-type immunosensor. *Biosens. Bioelectron.* **2018,** *102*, 301-306.

(28) Geng, H.; Chen, X.; Sun, L.; Qiao, Y.; Song, J.; Shi, S.; Cai, Q., ZnCuInSe/Au/TiO2 sandwich nanowires-based photoelectrochemical biosensor for ultrasensitive detection of kanamycin. *Anal. Chim. Acta* **2021,** *1146*, 166-173.

(29) Tan, F. R.; Wang, N.; Lei, D. Y.; Yu, W. X.; Zhang, X. M., Plasmonic Black Absorbers for Enhanced Photocurrent of Visible-Light Photocatalysis. *Adv. Opt. Mater.* **2017,** *5* (2).

(30) Guo, L.; Liang, K.; Marcus, K.; Li, Z.; Zhou, L.; Mani, P. D.; Chen, H.; Shen, C.; Dong, Y.; Zhai, L.; Coffey, K. R.; Orlovskaya, N.; Sohn, Y.-H.; Yang, Y., Enhanced Photoelectrocatalytic Reduction of Oxygen Using Au@TiO2 Plasmonic Film. *ACS Appl. Mater. Interfaces* **2016,** *8* (51), 34970-34977.

(31) Della Gaspera, E.; Karg, M.; Baldauf, J.; Jasieniak, J.; Maggioni, G.; Martucci, A., Au Nanoparticle Mono layers Covered with Sol-Gel Oxide Thin Films: Optical and Morphological Study. *Langmuir* **2011,** *27* (22), 13739-13747.

(32) Jiang, X.; Liu, H.; Sun, H.; Duan, L.; Zhao, X., Enhanced UV emission of TiO2-ZnO nanocomposite films synthesized by simplified sol-gel dip-coating method. *Mater. Express* **2018,** *8* (3), 288-293.

(33) Jia, H. P.; Wong, Y. L.; Jian, A. Q.; Tsoi, C. C.; Wang, M. L.; Li, W. H.; Zhang, W. D.; Sang, S. B.; Zhang, X. M., Microfluidic Reactors for Plasmonic Photocatalysis Using Gold Nanoparticles. *Micromachines* **2019,** *10* (12).

(34) Li, X.; Zhu, G. D.; Dou, J. L.; Yang, J. M.; Ge, Y. X.; Liu, J. Y., Electrospun Au nanoparticle-containing ZnO nanofiber for non-enzyme H2O2 sensor. *Ionics* **2019,** *25* (11), 5527-5536.

(35) Liu, Z.; Liu, X.; Huang, S.; Pan, P.; Chen, J.; Liu, G.; Gu, G., Automatically Acquired Broadband Plasmonic-Metamaterial Black Absorber during the Metallic Film-Formation. *ACS Appl. Mater. Interfaces* **2015,** *7* (8), 4962-4968.

(36) Cai, W.; Chettiar, U. K.; Yuan, H.-K.; de Silva, V. C.; Kildishev, A. V.; Drachev, V. P.; Shalaev, V. M., Metamagnetics with rainbow colors. *Opt. Express* **2007,** *15* (6), 3333-3341.

(37) Niu, J.; Shin, Y. J.; Son, J.; Lee, Y.; Ahn, J. H.; Yang, H., Shifting of surface plasmon resonance due to electromagnetic coupling between graphene and Au nanoparticles. *Opt. Express* **2012,** *20* (18), 19690-19696.

(38) Hedayati, M. K.; Javaherirahim, M.; Mozooni, B.; Abdelaziz, R.; Tavassolizadeh, A.; Chakravadhanula, V. S. K.; Zaporojtchenko, V.; Strunkus, T.; Faupel, F.; Elbahri, M., Design of a Perfect Black Absorber at Visible Frequencies Using Plasmonic Metamaterials. *Adv. Mater.* **2011,** *23* (45), 5410-+.

(39) Shi, X.; Ueno, K.; Oshikiri, T.; Sun, Q.; Sasaki, K.; Misawa, H., Enhanced water splitting under modal strong coupling conditions. *Nat. Nanotechnol.* **2018,** *13* (10), 953-+.

(40) Cao, Y.; Shi, X.; Oshikiri, T.; Zu, S.; Sunaba, Y.; Sasaki, K.; Misawa, H., Near-field engineering for boosting the photoelectrochemical activity to a modal strong coupling structure. *Chem. Commun.***2021,** *57* (4), 524-527.

(41) Xu, S.; Feng, X.; Gao, T.; Liu, G.; Mao, Y.; Lin, J.; Yu, X.; Luo, X., Aptamer induced multicoloured Au NCs-MoS2 "switch on" fluorescence resonance energy transfer biosensor for dual color simultaneous detection of multiple tumor markers by single wavelength excitation. *Anal. Chim. Acta* **2017,** *983*, 173-180.

(42) Chen, F.; Zhang, F.; Liu, Y.; Cai, C., Simply and sensitively simultaneous detection hepatocellular carcinoma markers AFP and miRNA-122 by a label-free resonance light scattering sensor. *Talanta* **2018,** *186*, 473-480.

(43) Lv, S.; Zhang, K.; Lin, Z.; Tang, D., Novel photoelectrochemical immunosensor for disease-related protein assisted by hemin/G-quadruplex-based DNAzyme on gold nanoparticles to enhance cathodic photocurrent on p-CuBi2O4 semiconductor. *Biosens. Bioelectron.* **2017,** *96*, 317-323.